

Delayed acceptance sampling with Hamiltonian proposal subchains for random field materials inference

Simona Béréšová^{1,2}, Michal Béréš^{1,2}, Tomáš Luber¹, and Stanislav Sysala¹

¹ Institute of Geonics of the Czech Academy of Sciences, Ostrava, Czech Republic

² Faculty of Electrical Engineering and Computer Science,
VŠB - Technical University of Ostrava, Ostrava, Czech Republic

June 16, 2026

Abstract

This paper focuses on accelerating Markov chain Monte Carlo (MCMC) sampling in Bayesian inverse problems in which forward model evaluations dominate the computational cost. It builds on several established ingredients that have previously been used successfully in related scenarios: delayed acceptance, neural network surrogate models, Hamiltonian proposals, and proposal subchains. The main algorithmic framework is the delayed-acceptance Metropolis-Hastings algorithm of Christen and Fox (2005). The first-stage proposal distribution is constructed from a subchain of Hamiltonian trajectories targeting the surrogate posterior. For each fixed surrogate model, the Hamiltonian subchain and delayed-acceptance correction define a kernel invariant with respect to the exact posterior. In the present work, the surrogate is updated only during a burn-in phase, after which the production run uses a fixed surrogate model.

The sampling framework is implemented in Python using parallel processes. Several chains are generated in parallel and share a single surrogate model trained during the burn-in phase on all collected data. The forward model is treated as a black box; therefore, the application area is broad. However, the main motivation behind this research is the efficient solution of geotechnical inverse problems with material properties represented by Gaussian random fields. In this study, the sampling framework is applied to a geotechnical inverse problem in which hydraulic conductivity and porosity are modeled as non-stationary Gaussian random fields (GRFs) approximated using a truncated Karhunen-Loeve expansion. Based on a precomputation, the truncation dimensions of the Karhunen-Loeve expansions are chosen separately for hydraulic conductivity and porosity. The forward model outputs are pore pressure values at the control points and selected observation times. These are compared with in situ pore pressure measurements collected over one year during the Tunnel Sealing Experiment conducted in an underground laboratory in Canada.

1 Introduction

Bayesian inversion has become an important tool in many areas of applied mathematics. It provides a natural way to integrate observational data with prior knowledge in order to quantify uncertainties in the unknown parameters via the posterior distribution. For posterior sampling, Markov chain Monte Carlo (MCMC) sampling methods are typical tools. In particular, the Metropolis-Hastings (MH) algorithm provides a robust mechanism for generating samples from complex posterior distributions. The MH algorithm is conceptually simple, requires minimal parameter tuning, and forms a simple building block for more advanced MCMC schemes. However, a major obstacle to the practical application of the classical MH algorithm is the computational cost of evaluating the forward model. In many applied fields, including geotechnics, hydrology, and structural mechanics, the forward model involves the numerical solution of a system of partial differential equations (PDEs) or other computationally demanding models. When each forward model evaluation requires several

seconds or minutes, naive MCMC becomes infeasible, especially in combination with high-dimensional unknown parameters.

Bayesian inversion with computationally expensive forward models has motivated a significant effort on the development of Markov chain Monte Carlo methods that reduce the number of exact model evaluations without sacrificing posterior correctness. A central idea in this literature is the delayed acceptance Metropolis-Hastings algorithm, introduced by Christen and Fox [6], where a cheap approximation is used to screen proposals before the expensive exact model is evaluated. The advantage of this approach is that it preserves the exact target distribution through a second-stage correction while reducing the cost of unsuccessful proposals.

Much effort has also been given to the use of various surrogate models for MCMC acceleration. For example, [11] showed that coarse models can be used to precondition sampling in expensive subsurface problems. Later, [9] proposed an adaptive delayed-acceptance strategy, demonstrating that an approximate forward model can be updated during sampling while the algorithm targets the exact posterior, and used this framework for geothermal reservoir calibration. For general-purpose settings with no obvious coarse model, [20] propose MCMC with an adaptive construction of a posterior approximation based on a weighted average of previous evaluations.

Another relevant topic concerns gradient-informed proposals, especially Hamiltonian Monte Carlo, see e.g. [16]. Hamiltonian methods were introduced in molecular simulation and later developed into a powerful MCMC methodology because they can generate distant proposals with relatively high acceptance probability, which substantially reduces random-walk behavior in correlated posterior distributions. The direction closest to the present paper is the intersection of delayed acceptance, surrogate modeling, and Hamiltonian proposals. The paper [10] combines neural network surrogate models, delayed acceptance, and Hamiltonian Monte Carlo for a PDE-based Bayesian inverse problem. The present paper uses a similar delayed-acceptance setting with one specific modification: the first-stage proposal is a finite subchain of Hamiltonian trajectories targeting an approximate posterior. The subchain strategy was successfully used by [14] within a multilevel delayed acceptance sampling scheme. Although that work is not specifically Hamiltonian, it directly supports the construction used here: if the inner kernel is reversible with respect to the approximate target, then the finite inner subchain can serve as a valid first-stage proposal in delayed acceptance.

The remaining theoretical issue is adaptation. Once the surrogate changes during the sampling process, we are using an adaptive MCMC algorithm, so stepwise exactness is not enough to guarantee ergodicity. This area is well studied; [2, 18, 1] provide the standard framework based on diminishing adaptation and containment conditions. In the present paper, every delayed-acceptance kernel with a frozen surrogate model targets the exact posterior. For online-trained neural network surrogates, the standard diminishing-adaptation and containment conditions are not satisfied. Therefore, the neural network is updated only during a burn-in phase, after which the surrogate model remains fixed. Future inspiration regarding controlled adaptation can be found e.g. in [7], which showed that changing local approximations can still lead to asymptotically exact sampling.

In the present paper, we combine delayed acceptance, finite Hamiltonian proposal subchains targeting a surrogate posterior distribution, and a neural-network surrogate model shared by several sampling processes. The shared surrogate model can be improved using collected data during the burn-in phase. This lets us study the method in a realistic PDE-constrained setting. The sampling framework is used within a Bayesian solution of a benchmark geotechnical inverse problem in which spatially varying material properties are represented by truncated Gaussian random fields.

2 Inverse problem in its general form

Consider a probability space $(\Xi, \mathcal{F}_\Xi, \mathbb{P})$ and the measurable spaces $(\mathbb{R}^n, \mathcal{B}(\mathbb{R}^n))$ and $(\mathbb{R}^m, \mathcal{B}(\mathbb{R}^m))$, where $n, m \in \mathbb{N}$. Let $G : \mathbb{R}^n \rightarrow \mathbb{R}^m$ be a measurable, deterministic forward model mapping

input parameters to model outputs. The aim of the inverse problem is to characterize the unknown model inputs corresponding to a given vector of noisy outputs $y \in \mathbb{R}^m$.

In practical applications, model outputs are not observed exactly due to measurement noise. Therefore, the observed data are modeled as a random variable $Y : \Omega \rightarrow \mathbb{R}^m$, and observational noise is represented by a random variable $Z : \Omega \rightarrow \mathbb{R}^m$. The unknown input parameters are modeled as a random variable $U : \Omega \rightarrow \mathbb{R}^n$. Throughout this paper, we assume that Z is independent of U . The relationship between these quantities is described by the additive noise model

$$Y = G(U) + Z. \quad (2.1)$$

A realization $y \in \mathbb{R}^m$ of Y is referred to as the observed data.

The Bayesian inverse problem consists of determining the conditional distribution of U given the observation $Y = y$, called the posterior distribution. In addition to the observational model, the Bayesian approach incorporates prior information about the unknown parameters in the form of a prior distribution, which reflects preliminary knowledge based on experience or modeling assumptions. Bayesian inference can thus be understood as a refinement of prior information using observed data.

We assume that the prior distribution of U and the noise distribution of Z admit probability density functions with respect to the Lebesgue measure on \mathbb{R}^n and \mathbb{R}^m , respectively. These densities are denoted by f_U and f_Z , and are referred to as the prior pdf and the noise pdf. The conditional pdf of Y given $U = u$ is denoted by $f_{Y|U}(y|u)$. For fixed y , the function $u \mapsto f_{Y|U}(y|u)$ is called the data likelihood.

Under the additive noise model assumption, the conditional density satisfies

$$f_{Y|U}(y|u) = f_Z(y - G(u)). \quad (2.2)$$

Given the observed data y , Bayes' theorem yields the posterior density

$$f_{U|Y}(u|y) = \frac{f_{Y|U}(y|u)f_U(u)}{\int_{\mathbb{R}^n} f_{Y|U}(y|v)f_U(v) dv} = \frac{f_Z(y - G(u))f_U(u)}{\int_{\mathbb{R}^n} f_Z(y - G(v))f_U(v) dv}. \quad (2.3)$$

We assume that the normalizing constant in the denominator is finite, ensuring that the posterior distribution is well defined. Using proportionality notation, the posterior density can be written as

$$f_{U|Y}(u|y) \propto \underbrace{f_Z(y - G(u))}_{\text{likelihood}} \underbrace{f_U(u)}_{\text{prior}} \quad (2.4)$$

almost everywhere with respect to the Lebesgue measure on \mathbb{R}^n .

Obtaining an explicit expression for the posterior density is only the first step in solving a Bayesian inverse problem. The main challenge is to make this expression computationally useful, for example by generating samples from the posterior distribution. Basic Monte Carlo sampling is not possible since the normalizing constant is unknown. Therefore, samples are typically generated using Markov chain Monte Carlo (MCMC) methods, which are described in Section 4.

3 Geotechnical benchmark problem

The geotechnical application considered in this paper is based on the tunnel-sealing experiment (TSX), performed in an underground research laboratory in Canada in 1997 and 1998; for a detailed description of this experiment, see the technical report [5]. It has previously been used as a benchmark for both forward and inverse modeling, see, e.g., [19, 13, 3]. The experiment was designed to allow two-dimensional modeling.

Figure 3.1a shows the problem geometry: the tunnel cross-section and the locations of the control points. The available data consist of four time series representing pore pressure measurements at these control points over one year, see Fig. 3.1b. For the purposes of the inverse problem, each time series was sampled at 18 uniformly distributed time points represented by dots in Fig. 3.1b. These samples define the observed data $y \in \mathbb{R}^{72}$. Observational

noise was chosen to be additive Gaussian with independent components $\mathcal{N}(0, (20\rho g)^2)$. The constants ρ and g provide the conversion from water-column height in meters to pressure in Pascals; they are defined in Table 3.2.

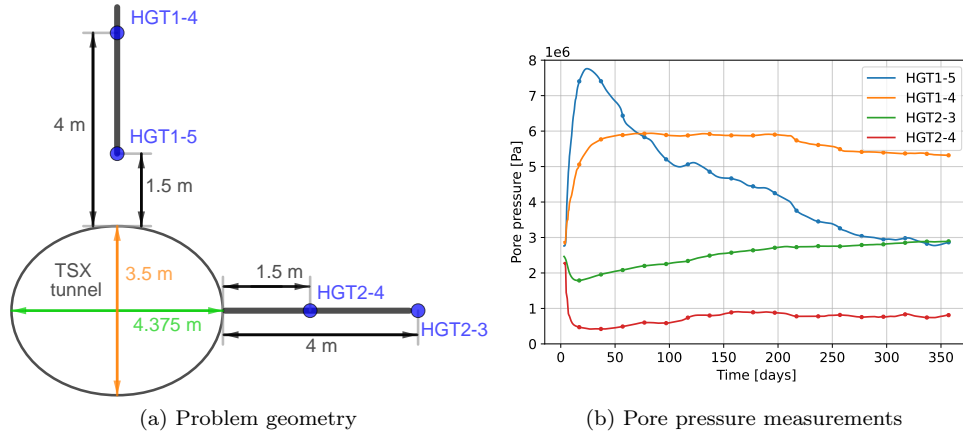


Figure 3.1: Problem geometry (tunnel cross-section and location of control points) and in-situ measurements (time series of pore pressure measurements at the control points)

3.1 PDE model

For the modeling of the hydro-mechanical processes around the tunnel, we consider the two-dimensional Biot poroelasticity model with zero volume forces given by equations

$$-\operatorname{div}(C : \varepsilon(u)) + \alpha_B \nabla p = 0 \quad (3.1)$$

$$S \frac{\partial p}{\partial t} - \nabla \cdot \left(\frac{K}{\rho g} \nabla p \right) + \alpha_B \frac{\partial}{\partial t} (\operatorname{div}(u)) = 0 \quad (3.2)$$

in $\Omega \subset \mathbb{R}^2$. Here, u is the displacement vector (in meters), p is pore pressure in Pascals, C is the elasticity tensor, ε is the small strain tensor

$$\varepsilon(u) = \frac{1}{2} \left(\nabla u + (\nabla u)^T \right),$$

and the elastic effective-stress term is

$$C : \varepsilon(u) = 2\mu\varepsilon(u) + \lambda \operatorname{div}(u) I$$

for an isotropic linear elastic medium; I is the identity tensor. Material parameters α_B , S , K , μ , λ and constants ρ , g will be specified in Section 3.2.

The domain Ω is a square $(-50, 50) \times (-50, 50)$ with an elliptic hole representing the tunnel cross-section, see Fig. 3.2. The ellipse is placed in the center of the square and its axes are parallel to the sides of the square. The lengths of the semi-axes are $r_x = 4.375/2$ m and $r_y = 3.5/2$ m. An unstructured mesh with $N = 1884$ nodes and 3664 triangular elements was chosen, and the time step is 0.5 day during the first 17 days and 2 days during the remaining part of the simulation (after excavation). This discretization is a compromise between accuracy and computational cost, and allows us to perform extensive numerical experiments in Section 5 for the sampling efficiency analysis.

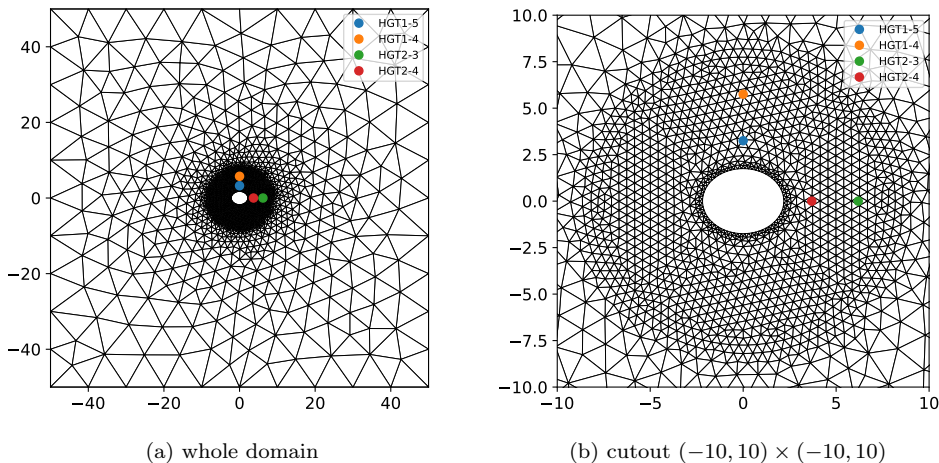


Figure 3.2: Discretization of $\Omega = (-50, 50) \times (-50, 50)$

We prescribe zero initial displacement $u_0 = 0$ m, initial pore pressure $p_0 = 4.1$ MPa, and the initial stress tensor given by the values $\sigma_x = 45$ MPa (stress close to horizontal), $\sigma_y = 12.8$ MPa (stress close to vertical) and angle $\omega = 8^\circ$ (representing rotation from the horizontal direction). These values are based on the technical report [5]. The boundary conditions prescribed on the inner elliptic hole simulate tunnel excavation during the first 17 days and the subsequent relaxation period (days 18 - 357). During the drilling period, the initial pore pressure and the initial stress transformed into the normal direction decrease linearly to zero. During the relaxation period, the pore pressure and the normal stress are equal to zero. Pore pressure on the outer square boundary is set to the ambient pore pressure value $p_0 = 4.1$ MPa.

From the results, we extract pore pressure values at the locations of the four control points and at the chosen time points corresponding to the vector of reference observations $y \in \mathbb{R}^{72}$.

3.2 Input material properties and their prior distribution

We consider uncertainty in the following material properties: hydraulic conductivity K , porosity ϕ , drained bulk modulus K_d , shear modulus μ , and grain bulk modulus K_s ; see Table 3.1. The prior distributions are chosen so that the parameter means and variances are consistent with the technical report [5], see the rest of this section. Fixed material properties and parameters of initial and boundary conditions are summarized in Table 3.2. Table 3.3 summarizes the remaining derived material properties that directly enter the PDEs.

| name and notation | unit | model | parameters |
|------------------------|-----------|--------------------------------|--|
| hydraulic conductivity | $K(x)$ | $\text{m} \cdot \text{s}^{-1}$ | (3.4) $\xi_1^K, \dots, \xi_{M_K}^K$ |
| porosity | $\phi(x)$ | - | (3.5) $\xi_1^\phi, \dots, \xi_{M_\phi}^\phi$ |
| drained bulk modulus | $K_d(x)$ | Pa | (3.6) $K_d^{\text{inner}}, K_d^{\text{outer}}$ |
| shear modulus | $\mu(x)$ | Pa | (3.7) $\mu^{\text{inner}}, \mu^{\text{outer}}$ |
| grain bulk modulus | K_s | Pa | spatially constant |

Table 3.1: Unknown material properties and their prior distribution, defined by $M_K + M_\phi + 5$ independent random variables; x is the spatial variable

| name | symbol, value, unit |
|---|--|
| fluid density | $\rho = 1000 \text{ kg} \cdot \text{m}^{-3}$ |
| gravitational acceleration | $g = 9.81 \text{ m} \cdot \text{s}^{-2}$ |
| stress, close to horizontal | $\sigma_x = 45 \text{ MPa}$ |
| stress, close to vertical | $\sigma_y = 12.8 \text{ MPa}$ |
| stress angle (rotation from horizontal) | $\omega = 8^\circ$ |
| initial (ambient) pore pressure | $p_0 = 4.1 \text{ MPa}$ |
| fluid bulk modulus | $K_f = 2.15 \text{ GPa}$ |

Table 3.2: Fixed material properties and parameters of initial/boundary conditions, based on the technical report [5]

| name | unit | formula |
|------------------------|------------------|--|
| Biot coefficient | - | $\alpha_B(x) = 1 - \frac{K_d(x)}{K_s}$ |
| storage coefficient | Pa^{-1} | $S(x) = \frac{\alpha_B(x) - \phi(x)}{K_s} + \frac{\phi(x)}{K_f}$ |
| Lamé's first parameter | Pa | $\lambda(x) = K_d(x) - \frac{2}{3}\mu(x)$ |

Table 3.3: Derived material properties entering the PDEs; x is the spatial variable

In contrast to previously used models [19, 3, 13], we model hydraulic conductivity and porosity using non-stationary Gaussian random fields (GRFs). The covariance function is

$$C(x_i, x_j) = \sigma(x_i)\sigma(x_j) \frac{2\ell(x_i)\ell(x_j)}{\ell(x_i)^2 + \ell(x_j)^2} \exp\left(-\frac{\|x_i - x_j\|^2}{\ell(x_i)^2 + \ell(x_j)^2}\right), \quad (3.3)$$

which is the non-stationary covariance construction from [17], where x_i, x_j are spatial coordinates, $\ell(x)$ is the spatially varying correlation length, and $\sigma(x)$ is the standard deviation. Here, the random fields are represented on the finite-element mesh. The covariance matrix $\mathbf{C} \in \mathbb{R}^{N \times N}$ has entries $\mathbf{C}_{ij} = C(x_i, x_j)$, where x_i and x_j are mesh nodes. Denote λ_m and \mathbf{v}_m its eigenpairs, and $\xi_m \sim \mathcal{N}(0, 1)$. The truncated Karhunen-Loeve (KL) expansion is then given in the nodal form as

$$g_M(x_i) = \sum_{m=1}^M \xi_m \sqrt{\lambda_m} \mathbf{v}_m(i), \quad M \leq N$$

for a mesh node x_i .

The functions $\ell(x)$ and $\sigma_K(x)$ and $\sigma_\phi(x)$ for hydraulic conductivity and porosity are defined as functions of the distance from the tunnel boundary, see Fig. 3.3. This yields truncated random fields $\text{GRF}_K^{M_K}(x)$ and $\text{GRF}_\phi^{M_\phi}(x)$ for K and ϕ . Figures 3.4 and 3.5 show random realizations of the GRFs and their truncated variants. The material fields $K(x)$ and $\phi(x)$ are then defined as

$$K(x) = 10^{\text{GRF}_K^{M_K}(x) - 13}, \quad (3.4)$$

$$\phi(x) = 10^{\text{GRF}_\phi^{M_\phi}(x) - 2.5}. \quad (3.5)$$

These random field representations define the prior distributions, i.e. $K(x)$ and $\phi(x)$ are represented using M_K and M_ϕ parameters.

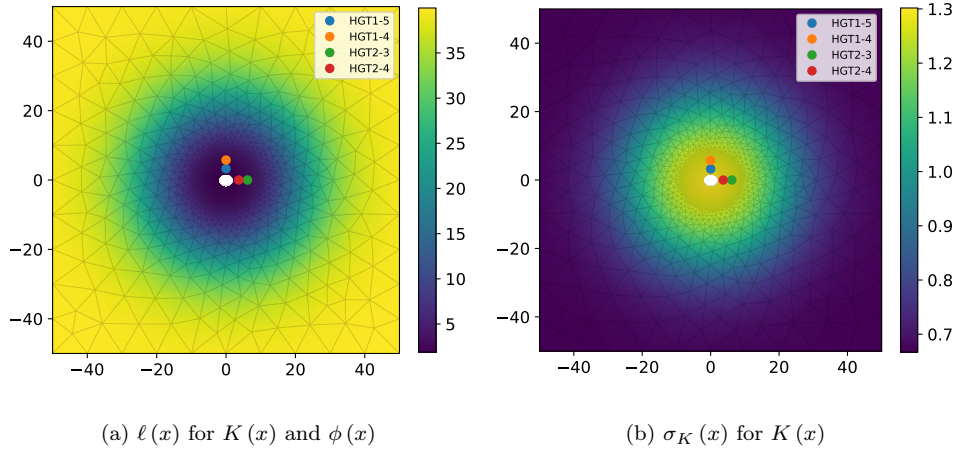


Figure 3.3: $\ell(x)$ field used both for hydraulic conductivity and porosity; $\sigma_K(x)$ field used for hydraulic conductivity (for porosity, constant $\sigma_\phi(x) = 0.5$ was chosen)

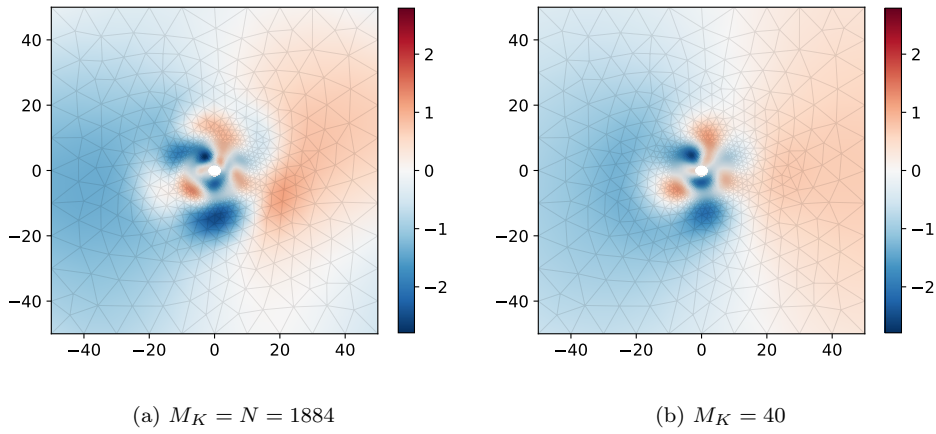


Figure 3.4: Random realization of $\text{GRF}_K^{M_K}(x)$ before and after truncation

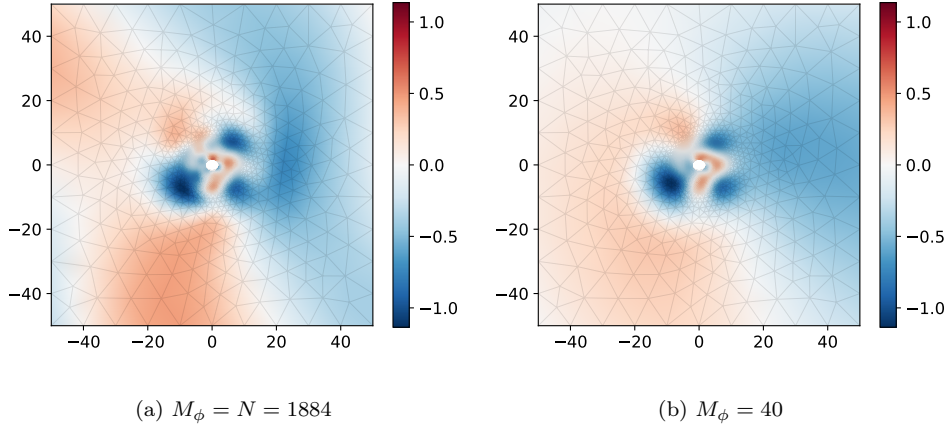


Figure 3.5: Random realization of $\text{GRF}_\phi^{M_\phi}(x)$ before and after truncation

It remains to specify prior distributions for K_d , μ , and K_s . K_s is assumed to be constant with prior distribution $\mathcal{N}(47, 2^2)$ in GPa. K_d and μ are expected to be lower in the excavation damaged zone (EDZ) and higher in the intact medium. Therefore, they are represented using two parameters each: one at the tunnel boundary and one at the outer boundary, with a smooth transition between them, see Fig. 3.6. The prior distributions of these parameters are

$$K_d^{\text{inner}} \sim \mathcal{N}(11, 1^2), K_d^{\text{outer}} \sim \mathcal{N}(13.5, 1^2), \quad (3.6)$$

$$\mu^{\text{inner}} \sim \mathcal{N}(14, 1^2), \mu^{\text{outer}} \sim \mathcal{N}(15.5, 1^2) \quad (3.7)$$

in GPa.

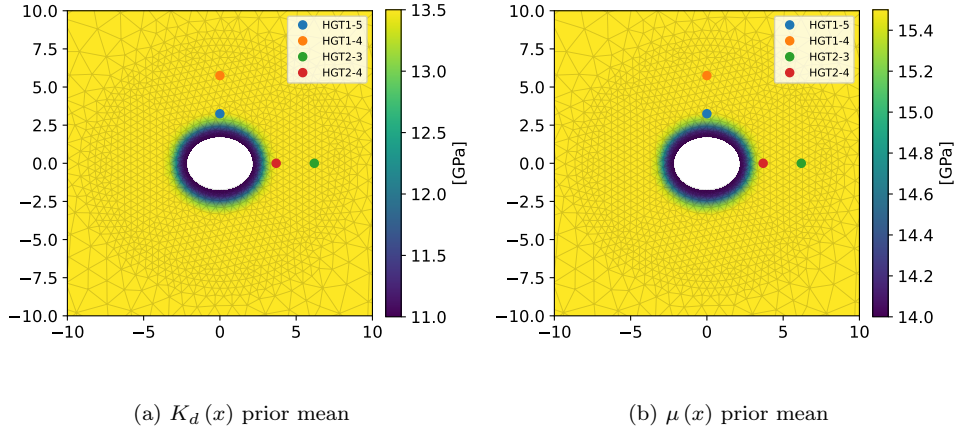


Figure 3.6: Prior mean fields of drained bulk modulus $K_d(x)$ and $\mu(x)$

This defines all input parameters of the forward model and the resulting prior distribution, consisting of $M_K + M_\phi + 5$ independent components. The choice of the truncation dimensions M_K and M_ϕ is discussed in the following subsection. Consequently, the forward map used in the Bayesian inverse problem has the form $G : \mathbb{R}^{M_K + M_\phi + 5} \rightarrow \mathbb{R}^{72}$. At this point, all components of the Bayesian inverse problem are defined: y , G , likelihood, prior, and the posterior distribution given by the formula (2.4).

3.3 Choice of truncation dimensions

For a Gaussian random field, the first preliminary choice of truncation dimension can be based on the cumulative variance captured by the retained KL modes. If \mathbf{C} has eigenvalues $\lambda_1 \geq \lambda_2 \geq \dots$, then the total prior variance of the GRF is given by the sum of all eigenvalues, so the fraction of variance captured by the first M modes is

$$\frac{\sum_{m=1}^M \lambda_m}{\sum_{m=1}^N \lambda_m}.$$

Using this criterion on $\text{GRF}_K^{M_K}(x)$ and $\text{GRF}_\phi^{M_\phi}(x)$ gives the following thresholds: For the hydraulic conductivity field, 30 modes capture approximately 95% of variance and 53 modes 99% of variance. For the porosity field, 32 modes capture approximately 95% of variance and 56 modes 99%.

For the final decision, we also considered a likelihood-informed criterion. A parameter vector with the largest posterior density among the samples found so far was used as a *best posterior sample*. Perturbations around this sample were then generated using $\mathcal{N}(0, 0.01^2)$ and $\mathcal{N}(0, 0.1^2)$, and the resulting likelihood responses were compared under different truncation levels. Hydraulic-conductivity parameters and porosity parameters were perturbed separately; see Fig. 3.7. Based on this study, $M_K = M_\phi = 40$ was chosen as a sufficient number of modes. Therefore, in what follows, we work with the forward map $G : \mathbb{R}^{85} \rightarrow \mathbb{R}^{72}$.

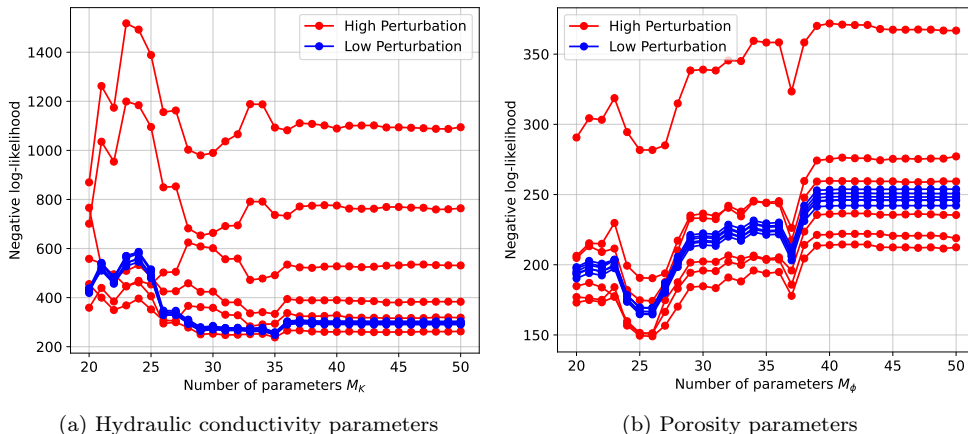


Figure 3.7: Likelihood-informed truncation study

4 Sampling framework

This section introduces the main sampling ingredients and then combines them in the delayed-acceptance Hamiltonian Monte Carlo (DAHMC) algorithm with subchains.

4.1 Metropolis-Hastings

We begin with the basic Metropolis-Hastings (MH) algorithm, since all later methods in this section build on it. Let $f : \mathbb{R}^n \rightarrow \mathbb{R}$ denote the unnormalized posterior density, and let $q(\cdot|u)$ be a proposal density. Given the current state $u^{(k)}$, the MH algorithm (Alg. 1) draws a proposal v from $q(\cdot|u^{(k)})$ and accepts it with probability

$$a(u^{(k)}, v) = \min\left(1, \frac{q(u^{(k)}|v) f(v)}{q(v|u^{(k)}) f(u^{(k)})}\right).$$

If the proposal is accepted, then $u^{(k+1)} = v$; otherwise, $u^{(k+1)} = u^{(k)}$. This acceptance rule ensures detailed balance with respect to the target distribution and therefore preserves the

posterior distribution as the invariant distribution of the resulting Markov chain. When the proposal density is symmetric, the ratio of proposal densities cancels and the method reduces to the original Metropolis algorithm [15]; the general Metropolis-Hastings form follows [12].

The efficiency of the MH algorithm strongly depends on the choice of the proposal density. If proposals are too conservative (e.g. random walk with small variance), the chain mixes slowly because of high autocorrelation. If they are too aggressive (e.g. random walk with high variance), the acceptance rate becomes too low. In inverse problems driven by computationally intensive forward models, the main drawback is that each proposal (either accepted or rejected) requires an evaluation of the full forward model. This motivates the use of the delayed-acceptance principle reviewed next.

Algorithm 1 Metropolis-Hastings algorithm

Given: target density $f : \mathbb{R}^n \rightarrow \mathbb{R}$, proposal density q , initial state $u^{(0)}$ with $f(u^{(0)}) > 0$.

- 1: **for** $k = 0, 1, \dots$ **do**
 - 2: Draw $v \sim q(\cdot | u^{(k)})$.
 - 3: Accept the proposal with the acceptance probability

$$a(u^{(k)}, v) = \min\left(1, \frac{q(u^{(k)} | v) f(v)}{q(v | u^{(k)}) f(u^{(k)})}\right).$$
 - 4: **if** the proposal is accepted **then**
 - 5: Set $u^{(k+1)} = v$.
 - 6: **else**
 - 7: Set $u^{(k+1)} = u^{(k)}$.
 - 8: **end if**
 - 9: **end for**
-

4.2 Delayed acceptance Metropolis-Hastings

When the dominant computational cost arises from evaluating the forward model, it is natural to introduce a cheap approximation of the target density. Delayed acceptance Metropolis-Hastings (DAMH), introduced by Christen and Fox [6], uses such an approximation to reject unpromising proposals before the expensive forward model is evaluated.

Let $\tilde{f} : \mathbb{R}^n \rightarrow \mathbb{R}$ denote an approximate unnormalized posterior density such that $\text{supp } \tilde{f} \supset \text{supp } f$, for details on DAMH requirements see [3]. Given the current state $u^{(k)}$ and a proposal $v \sim q(\cdot | u^{(k)})$, the first stage accepts the proposal with probability

$$a_{Q, \tilde{\mu}}(u^{(k)}, v) = \min\left(1, \frac{q(u^{(k)} | v) \tilde{f}(v)}{q(v | u^{(k)}) \tilde{f}(u^{(k)})}\right).$$

The exact density $f(v)$ is evaluated only if the proposal passes this preliminary test. The second-stage acceptance probability is then

$$a_{\tilde{Q}, \mu}(u^{(k)}, v) = \min\left(1, \frac{\tilde{f}(u^{(k)}) f(v)}{\tilde{f}(v) f(u^{(k)})}\right).$$

This two-stage construction preserves the correct posterior distribution while reducing the number of expensive evaluations of the full forward model, see Alg. 2. In the present paper, the approximation \tilde{f} is induced by a surrogate approximation of the forward map G .

Algorithm 2 Delayed acceptance Metropolis-Hastings algorithm

Given: exact density f , surrogate density \tilde{f} , proposal density q , initial state $u^{(0)}$

- 1: with $f(u^{(0)}) > 0$.
 - 2: **for** $k = 0, 1, \dots$ **do**
 - 3: Draw $v \sim q(\cdot | u^{(k)})$.
 - 4: Accept the proposal with the first-stage acceptance probability
$$a_{Q, \tilde{\mu}}(u^{(k)}, v) = \min\left(1, \frac{q(u^{(k)} | v) \tilde{f}(v)}{q(v | u^{(k)}) \tilde{f}(u^{(k)})}\right).$$
 - 5: **if** the first stage accepts **then**
 - 6: Evaluate the exact density $f(v)$.
 - 7: Accept the proposal with the second-stage acceptance probability
$$a_{\tilde{Q}, \mu}(u^{(k)}, v) = \min\left(1, \frac{\tilde{f}(u^{(k)}) f(v)}{\tilde{f}(v) f(u^{(k)})}\right).$$
 - 8: **if** the second stage accepts **then**
 - 9: Set $u^{(k+1)} = v$.
 - 10: **else**
 - 11: Set $u^{(k+1)} = u^{(k)}$.
 - 12: **end if**
 - 13: **else**
 - 14: Set $u^{(k+1)} = u^{(k)}$.
 - 15: **end if**
 - 16: **end for**
-

4.3 pCN proposal

The preconditioned Crank-Nicolson (pCN) proposal [8] is a dimension-robust alternative to random-walk proposals. In this work, it serves as a baseline for comparison, not as a main ingredient of the proposed sampling framework. For a Gaussian prior, pCN is reversible with respect to the prior. If u denotes the current state and $\xi \sim \mathcal{N}(0, C_0)$ an independent Gaussian prior draw, then the pCN proposal is

$$v = \sqrt{1 - \beta^2} u + \beta \xi, \quad \beta \in (0, 1].$$

Compared with random-walk proposals, pCN has one main tuning parameter β . This is convenient in practice; however, the choice of β still strongly influences acceptance and mixing.

4.4 Hamiltonian proposal

The efficiency of MH-based algorithms strongly depends on the proposal strategy. For high-dimensional and strongly correlated posterior distributions, random-walk proposals often lead to slow exploration of the state space due to high autocorrelation of the resulting chain. Improving mixing has two main aspects:

1. The proposed sample should be “distant” from the original sample to reduce correlation.
2. The acceptance probability should be high, so the chain has a low probability of staying in the original position.

To address both objectives, we consider the Hamiltonian proposal according to [16]. The key idea is to augment the parameter vector by an auxiliary momentum vector and to generate proposals by approximately following a Hamiltonian trajectory. Long Hamiltonian trajectories allow distant proposals, which is the first aspect of the decorrelation goal.

Let $u \in \mathbb{R}^n$ denote the parameter vector and let $p \in \mathbb{R}^n$ be an auxiliary momentum variable with distribution $\mathcal{N}(0, M)$. Here, M is a symmetric positive-definite mass matrix.

Define the potential energy $\mathcal{U}(u) = -\log f(u)$ up to an additive constant, the kinetic energy $\mathcal{K}(p) = \frac{1}{2}p^T M^{-1}p$, and the Hamiltonian

$$\mathcal{H}(u, p) = \mathcal{U}(u) + \mathcal{K}(p).$$

The continuous Hamiltonian dynamics are given by

$$\frac{du}{dt} = M^{-1}p, \quad \frac{dp}{dt} = -\nabla\mathcal{U}(u).$$

Their exact flow preserves the Hamiltonian and is volume preserving, which makes it suitable for constructing proposals in the Metropolis-Hastings algorithm.

In computations, the continuous dynamics are replaced by a reversible and volume-preserving symplectic integrator, typically the leapfrog scheme. Starting from the current state $u^{(k)}$, one first draws a fresh momentum $p^{(0)} \sim \mathcal{N}(0, M)$ and then performs L leapfrog steps with step size $\varepsilon > 0$:

$$p^{(\ell+\frac{1}{2})} = p^{(\ell)} - \frac{\varepsilon}{2}\nabla\mathcal{U}(u^{(\ell)}),$$

$$u^{(\ell+1)} = u^{(\ell)} + \varepsilon M^{-1}p^{(\ell+\frac{1}{2})},$$

$$p^{(\ell+1)} = p^{(\ell+\frac{1}{2})} - \frac{\varepsilon}{2}\nabla\mathcal{U}(u^{(\ell+1)}), \quad \ell = 0, \dots, L-1.$$

Then, $(v, -p^{(L)})$ is taken as the proposal. The momentum flip makes the numerical Hamiltonian map reversible, while $\mathcal{K}(p) = \mathcal{K}(-p)$, so the acceptance probability is numerically unchanged. The resulting proposal is accepted with probability

$$a_{\text{HMC}}\left(\left(u^{(k)}, p^{(0)}\right), \left(v, -p^{(L)}\right)\right) = \min\left(1, \exp\left(-\mathcal{H}\left(v, -p^{(L)}\right) + \mathcal{H}\left(u^{(k)}, p^{(0)}\right)\right)\right). \quad (4.1)$$

If the numerical integration were exact, this acceptance probability would equal one. In practice, the correction compensates for the discretization error introduced by the leapfrog approximation but remains close to 1, which is the second aspect of the decorrelation goal.

In the proposed sampling framework, Hamiltonian trajectories are not used directly with the full forward model. Instead, they are generated using a surrogate-based approximation of the target and serve as an efficient first-stage proposal mechanism inside the delayed-acceptance framework. With a fixed surrogate model, this is an ordinary delayed-acceptance proposal and the second-stage correction preserves the exact posterior. Surrogate updates, if used, are confined to burn-in. The discussion so far is finite-dimensional, with the unknown represented by a vector in \mathbb{R}^n . A dimension-robust Hamiltonian proposal can also be defined in function space, similarly to pCN, see [4].

4.5 Subchain of Hamiltonian proposals

The delayed-acceptance framework can be generalized by replacing the single first-stage proposal with a short subchain targeting the approximate posterior distribution. This perspective is closely related to [14]. Let $\tilde{\mu}$ denote the approximate posterior measure with density proportional to \tilde{f} , and let \tilde{K} be a Markov transition kernel reversible with respect to $\tilde{\mu}$. Starting from the current outer state $u^{(k)}$, define an inner chain by $w^{(0)} = u^{(k)}$ and generate $w^{(1)}, \dots, w^{(J)}$ using the kernel \tilde{K} . The endpoint $v = w^{(J)}$ is then used as the first-stage proposal for the exact target. In other words, the usual proposal density is replaced by the J -step kernel \tilde{K}^J .

This replacement leads to a particularly simple acceptance formula. Since \tilde{K} is reversible with respect to $\tilde{\mu}$, the same is true for \tilde{K}^J , that is,

$$\tilde{f}(u) \tilde{K}^J(u, dv) = \tilde{f}(v) \tilde{K}^J(v, du).$$

Therefore, if the outer chain targeting the exact density f uses \tilde{K}^J as its proposal kernel, then the second-stage acceptance probability has the standard form

$$a_{\text{DA}}(u, v) = \min\left(1, \frac{\tilde{f}(u) f(v)}{\tilde{f}(v) f(u)}\right).$$

The detailed balance condition for the outer chain follows immediately from the reversibility of \tilde{K}^J :

$$f(u) a_{\text{DA}}(u, v) \tilde{K}^J(u, dv) = f(v) a_{\text{DA}}(v, u) \tilde{K}^J(v, du).$$

Hence, the endpoint of a finite subchain targeting the surrogate posterior can be used as a valid proposal for the exact posterior.

In the general discussion above, \tilde{K} may be any reversible kernel targeting the approximate posterior $\tilde{\mu}$. Here, we consider an MH kernel with a Hamiltonian proposal targeting $\tilde{\mu}$.

4.6 DAHMC algorithm with subchains

Combining the previous ingredients leads to the DAHMC algorithm with subchains. In each outer iteration, a fixed-length Hamiltonian subchain targeting the surrogate posterior is constructed, and the endpoint of that subchain is then corrected by delayed acceptance with respect to the exact posterior.

The surrogate model is fixed within each outer iteration: all surrogate likelihoods, gradients, inner HMC decisions, and delayed-acceptance ratios in one outer iteration use the same fixed surrogate model. Retraining affects only later iterations during burn-in.

Algorithm 3 DAHMC algorithm with Hamiltonian proposal subchains

Given: exact density f , initial surrogate density $\tilde{f}^{(0)}$, subchain length J ,
1: leapfrog step size ε , leapfrog step count L , mass matrix M , initial state $u^{(0)}$.
2: **for** $k = 0, 1, \dots$ **do**
3: Set $w^{(0)} = u^{(k)}$.
4: **for** $j = 0, \dots, J - 1$ **do**
5: Draw $p^{(0)} \sim \mathcal{N}(0, M)$.
6: Compute L surrogate-driven leapfrog steps of size ε starting from $(w^{(j)}, p^{(0)})$
7: and ending in $(z, p^{(L)})$.
8: Accept z with the Hamiltonian acceptance probability from Eq. (4.1).
9: **if** z is accepted **then**
10: Set $w^{(j+1)} = z$.
11: **else**
12: Set $w^{(j+1)} = w^{(j)}$.
13: **end if**
14: **end for**
15: Set $v = w^{(J)}$.
16: Accept the proposal with the second-stage acceptance probability

$$a_{\text{DA}}(u^{(k)}, v) = \min\left(1, \frac{\tilde{f}^{(k)}(u^{(k)}) f(v)}{\tilde{f}^{(k)}(v) f(u^{(k)})}\right).$$

17: **if** the second stage accepts **then**
18: Set $u^{(k+1)} = v$.
19: **else**
20: Set $u^{(k+1)} = u^{(k)}$.
21: **end if**
22: Set $\tilde{f}^{(k+1)}$ either as $\tilde{f}^{(k)}$ or its update.
23: **end for**

4.7 Parallel scheme with surrogate retraining

The sampling framework is implemented as a parallel delayed-acceptance scheme in which multiple sampling processes share one surrogate model. Each sampler generates its own

Markov chain and requests exact forward model solutions only when needed by the delayed-acceptance correction. The resulting parameter-observation snapshots are sent to a collector process, which accumulates the training data and retrains the neural-network surrogate model. Figure 4.1 shows a schematic communication diagram between samplers, the collector, and the surrogate-updater module. The updated surrogate models are distributed to the samplers only during the burn-in phase.

In the current setting, the surrogate is a fully connected PyTorch multilayer perceptron (MLP) with three hidden layers of width 256 and SiLU activation functions. The outputs are normalized by a fixed mean vector and scale vector derived from the reference observations. The main advantage of choosing a MLP as a surrogate model is the simplicity of obtaining derivatives of the approximate forward map through automatic differentiation. This makes gradient-based proposals such as Hamiltonian subchains straightforward to implement. Its main disadvantage is the relatively large number of hyperparameters that must be tuned, including architecture and training process settings.

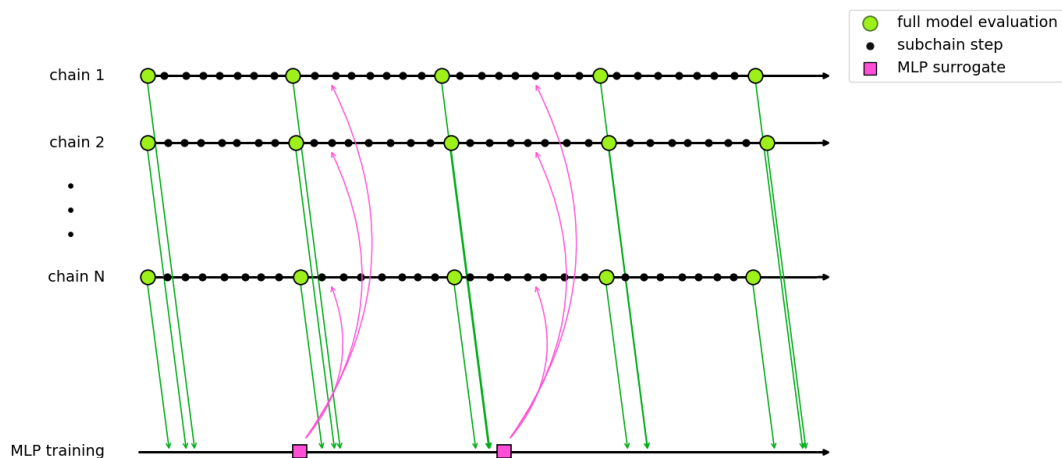


Figure 4.1: Parallel sampling architecture with sampler processes, a shared collector, and surrogate retraining.

5 Sampling efficiency

Sampling efficiency is assessed by how many effectively independent posterior samples are obtained for a given computational cost. In practice, we estimate this through the integrated autocorrelation time (IAT) and the corresponding effective sample size (ESS). Lower autocorrelation and larger ESS indicate more efficient exploration of the posterior. The IAT tends to be underestimated when only short chains are available, so the results in this section should be read as practical finite-run diagnostics rather than exact asymptotic quantities.

The numerical comparison in this section considers three samplers: DAHMC, DAMH with a pCN subchain, and MH with a pCN proposal and no surrogate. The tuning parameters were fixed after burn-in, including the pCN parameter, the pretrained MLP surrogate, and the HMC mass matrix.

For DAHMC with subchain length J , leapfrog count L , full model cost c_F , surrogate evaluation cost c_E , surrogate gradient cost c_J , and probability p_{move} that at least one inner proposal is accepted, the cost of one outer step is approximated by

$$T_{\text{step}}(J, L) \approx J((L + 1)c_J + c_E) + p_{\text{move}}c_F.$$

For the present TSX benchmark, we take $c_F \approx 854.7$ ms, $c_E \approx 0.051$ ms, and $c_J \approx 0.729$ ms for the pretrained fixed MLP.

The results presented in Section 6 are based on a run with the following settings: $J = 25$, $\varepsilon = 0.08$, $L = 20$. Since $p_{\text{move}} = 1$ in the reported run, the outer step cost is

$$T_{\text{step}}(25, 20) \approx 854.7 + 25(0.729 \cdot 21 + 0.051) \approx 1239 \text{ ms.}$$

The estimated IAT was $\tau = 23$. Therefore, the cost per effective sample corresponded approximately to the cost of $\frac{\tau}{c_F} T_{\text{step}}(25, 20) \approx 33.4$ evaluations of the full model.

For the pCN subchain run, $\beta = 0.07$ and $J = 100$ were used, and the step cost was

$$T_{\text{step}}^{\text{pCN}}(J) \approx J c_E + p_{\text{move}} c_F = 860 \text{ ms.}$$

The estimated IAT was $\tau = 125$ and $p_{\text{move}} = 1$. Therefore, the cost per effective sample corresponded approximately to the cost of $\frac{\tau}{c_F} T_{\text{step}}^{\text{pCN}}(100) \approx 125.8$ evaluations of the full model. Relative to the DAHMC cost above, this corresponds to a DAHMC speedup factor of about 3.8 over the pCN-subchain variant.

In the case of the pure MH run with pCN proposal and $\beta = 0.07$, a reliable IAT estimate was not obtained because of the limited chain length. We therefore report only the qualitative conclusion that the IAT (i.e., the cost per effective sample measured in full-model evaluations) was larger than 2000. Relative to the DAHMC cost above, this corresponds to a DAHMC speedup factor of more than 60 over the pure MH baseline.

6 Posterior distribution description

This section contains the analysis of the posterior distribution of the benchmark problem using samples obtained by MCMC methods. The forward model, inverse problem formulation, and sampling efficiency were discussed in previous sections. Here, we focus on the structure of the posterior itself, the marginal behavior, and the induced uncertainty in the spatial fields.

The parameter space consists of the $M_K = 40$ hydraulic-conductivity KL coefficients, the $M_\phi = 40$ porosity KL coefficients, and the five scalar mechanical parameters. The prior distribution has independent components. Internally, the sampling framework uses prior components transformed into $\mathcal{N}(0, 1)$. This affects only the five scalar parameters; the KL coefficient priors are already standard normal.

A basic view is provided by the correlation and covariance matrices in the internal coordinates; see Figures 6.1a and 6.1b. We can observe couplings among the KL coefficients and between the field coefficients and the scalar mechanical parameters.

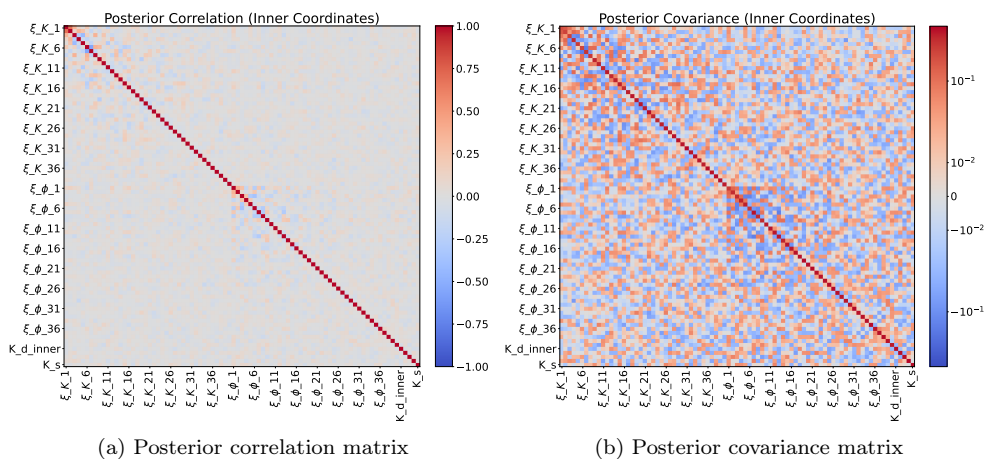


Figure 6.1: Posterior correlation and covariance matrix in inner coordinates

The KL coefficients associated with K and ϕ are summarized by box-whisker plots in Figures 6.2 and 6.3. The boxes show the interquartile range, whiskers indicate the 5% and 95% quantiles, the horizontal line is the median, and the cross marks the posterior mean. Several leading modes are clearly shifted away from zero, indicating non-negligible posterior updating in both fields, compared to the standard Gaussian priors.

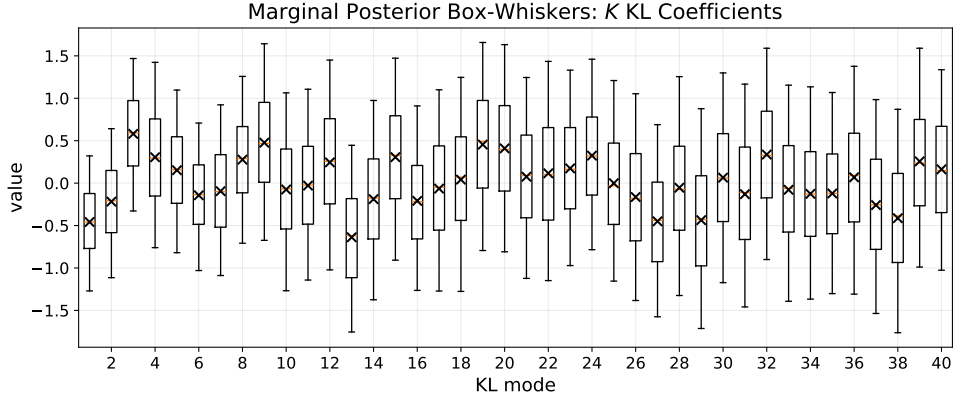


Figure 6.2: Marginal posterior distributions for the hydraulic conductivity KL coefficients

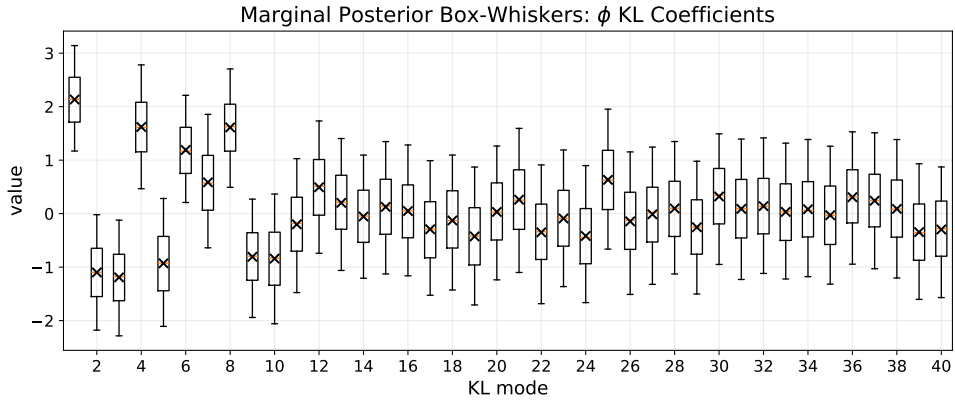


Figure 6.3: Marginal posterior distributions for the porosity KL coefficients

The scalar parameters are summarized in Figure 6.4, where the posterior marginals are compared directly with the Gaussian priors. The posterior means are $K_d^{\text{inner}} = 11.02$ GPa, $K_d^{\text{outer}} = 13.83$ GPa, $\mu^{\text{inner}} = 14.00$ GPa, $\mu^{\text{outer}} = 15.60$ GPa, and $K_s = 47.03$ GPa. The corresponding posterior standard deviations are approximately 0.78 GPa, 0.78 GPa, 0.80 GPa, 0.84 GPa, and 1.58 GPa. These values remain close to the prior means, but the posterior marginals are visibly sharpened relative to the prior densities, indicating moderate information gain in the scalar mechanical parameters.

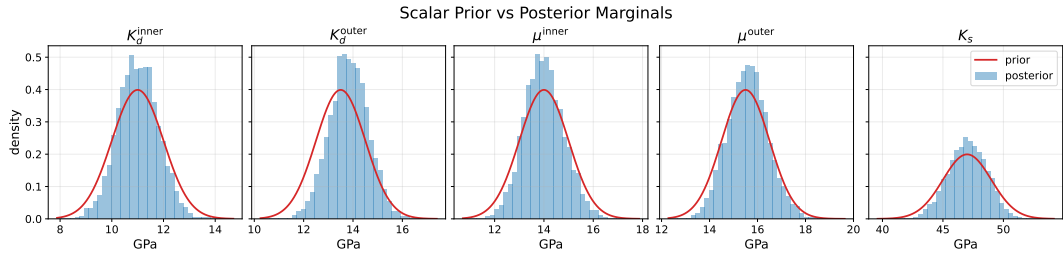


Figure 6.4: Prior-to-posterior comparison for the scalar mechanical parameters

Spatial posterior fields in the logarithmic parameterization. Because the parameterization is built in terms of KL expansions of the logarithmic fields, the most direct spatial interpretation is obtained from the posterior moments of $\log_{10} K$ and $\log_{10} \phi$. Figures 6.5 and 6.6 show the posterior mean and posterior standard deviation of these fields on the full computational domain and in a local tunnel-centered cutout. The figures show significant spatial heterogeneity in both the posterior mean and the posterior uncertainty. The cutout view makes the near-tunnel spatial structure easier to inspect and shows that the posterior information depends strongly on the location of the control points.

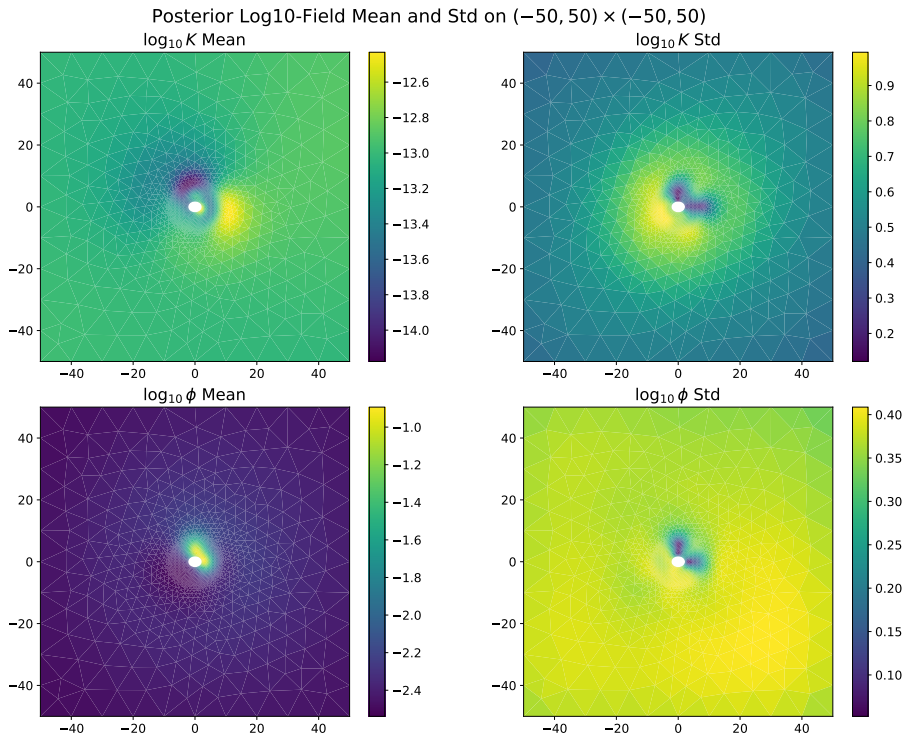


Figure 6.5: Posterior mean and posterior standard deviation of $\log_{10} K$ and $\log_{10} \phi$ on the full computational domain

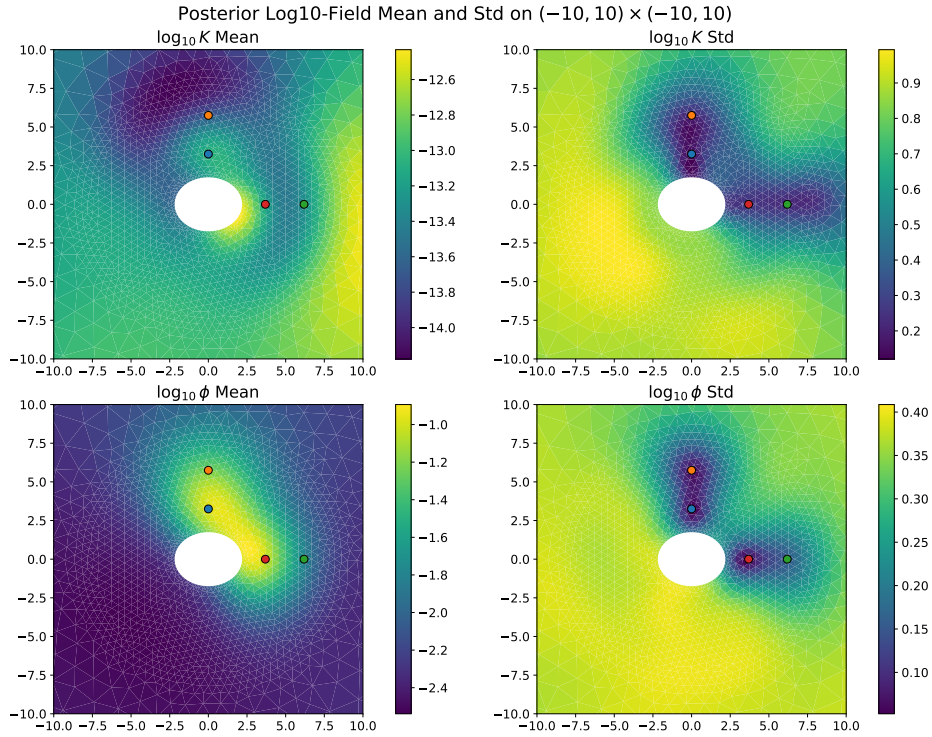


Figure 6.6: Posterior mean and posterior standard deviation of $\log_{10} K$ and $\log_{10} \phi$ in a tunnel-centered cutout

Best fit. Finally, Figure 6.7 shows the response of the sample with the largest data likelihood among the collected samples against the observed data $y \in \mathbb{R}^{72}$, i.e. the pore-pressure time series. Searching for a best fitting sample is not the primary outcome of the Bayesian inverse analysis. Nevertheless, it provides a useful diagnostic: it demonstrates that the posterior support contains parameter configurations capable of reproducing the observation trends reasonably well.

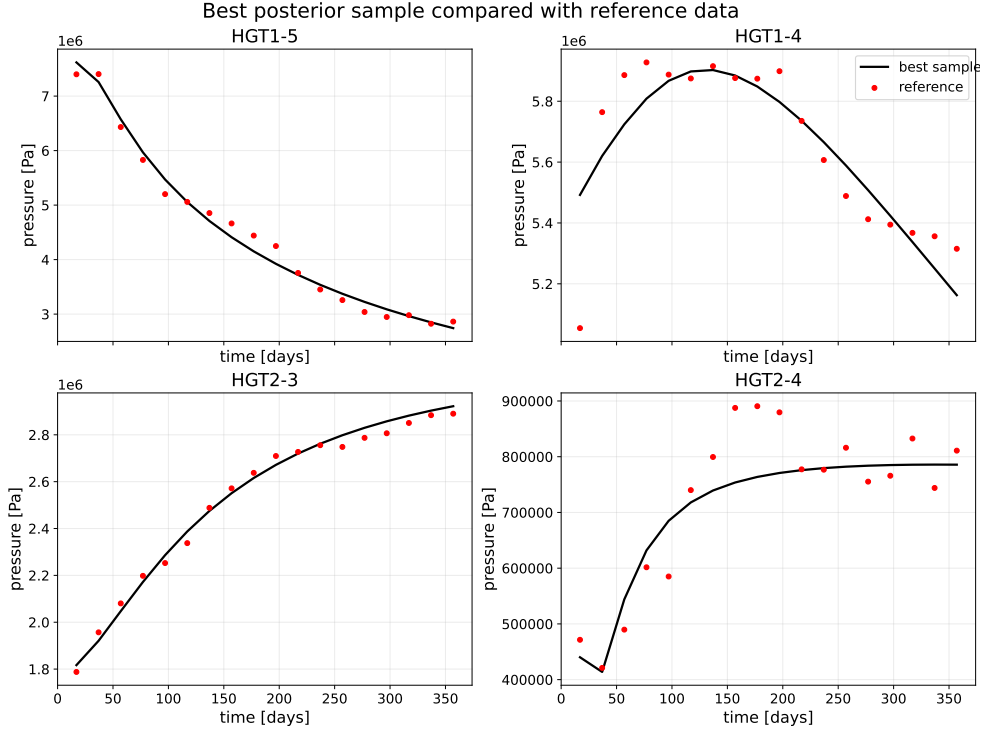


Figure 6.7: Best posterior sample compared with the reference data

7 Conclusions

This paper studied delayed-acceptance sampling with Hamiltonian proposal subchains for Bayesian inverse problems with expensive forward models. The method combines surrogate-based screening, Hamiltonian proposals, and finite subchains within an exact delayed-acceptance correction, while the surrogate is updated only during burn-in and then fixed for production sampling.

The practical advantage comes from using cheap surrogate derivatives obtained through automatic differentiation of the MLP surrogate to build longer and more informative first-stage moves. At the same time, neural-network derivatives may be less stable, especially during training, which is one reason why the subchain construction is useful as a robust practical variant.

The TSX benchmark allowed us to test the sampling framework in a realistic PDE-based setting. The resulting DAHMC sampler was substantially more efficient than the basic MH baseline (more than 60 times) and also clearly improved over the pCN-subchain variant (about 3.8 times). However, the TSX forward model is not expensive enough to fully expose the potential of surrogate-based acceleration, so the gains observed here should be interpreted as conservative. Future work should therefore include more expensive forward models, stronger diagnostics, and a deeper study of adaptive surrogate model updates.

Acknowledgements

This work was supported by the European Union under Grant Agreement no 101166718 (EURAD-2 project).

The research was co-funded by the European Union under the project INODIN, no. CZ.02.01.01/00/23_020/0008487.

This article was co-funded by the European Union under the REFRESH - Research Excellence For REgion Sustainability and High-tech Industries project number CZ.10.03.01/00/22_003/0000048 via the Operational Programme Just Transition.

References

- [1] Christophe Andrieu and Eric Moulines. On the ergodicity properties of some adaptive mcmc algorithms. *The Annals of Applied Probability*, 16(3), 2006.
- [2] Yan Bai, Gareth O. Roberts, and Jeffrey S. Rosenthal. On the containment condition for adaptive Markov chain Monte Carlo algorithms. *Advances and Applications in Statistics*, 21(1):1–54, 2011.
- [3] Simona Bérešová. *Bayesian approach to the identification of parameters of differential equations*. Phd thesis, Vysoká škola báňská – Technická univerzita Ostrava, 2022.
- [4] Alexandros Beskos, Frank J. Pinski, Jesus Maria Sanz-Serna, and Andrew M. Stuart. Hybrid monte carlo on hilbert spaces. *Stochastic Processes and their Applications*, 121(10):2201–2230, 2011.
- [5] N. A. Chandler, A. Cournot, and D. Dixon. The five year report of the Tunnel Sealing Experiment: an international project of AECL, JNC, ANDRA and WIPP, July 2002.
- [6] J. Andrés Christen and Colin Fox. Markov chain Monte Carlo Using an Approximation. *Journal of Computational and Graphical Statistics*, 14(4):795–810, December 2005.
- [7] Patrick R. Conrad, Youssef M. Marzouk, Natesh S. Pillai, and Aaron Smith. Accelerating Asymptotically Exact MCMC for Computationally Intensive Models via Local Approximations. *Journal of the American Statistical Association*, 111(516):1591–1607, October 2016.
- [8] Simon L. Cotter, Gareth O. Roberts, Andrew M. Stuart, and David White. Mcmc methods for functions: Modifying old algorithms to make them faster. *Statistical Science*, 28(3):424–446, 2013.
- [9] T. Cui, C. Fox, and M. J. O’Sullivan. Bayesian calibration of a large-scale geothermal reservoir model by a new adaptive delayed acceptance Metropolis Hastings algorithm: ADAPTIVE DELAYED ACCEPTANCE METROPOLIS-HASTINGS ALGORITHM. *Water Resources Research*, 47(10), October 2011.
- [10] Teo Deveney, Eike H. Mueller, and Tony Shardlow. Deep surrogate accelerated delayed-acceptance hamiltonian monte carlo for bayesian inference of spatio-temporal heat fluxes in rotating disc systems. *SIAM/ASA Journal on Uncertainty Quantification*, 11(3):970–995, 2023.
- [11] Y. Efendiev, T. Hou, and W. Luo. Preconditioning Markov Chain Monte Carlo Simulations Using Coarse-Scale Models. *SIAM Journal on Scientific Computing*, 28(2):776–803, January 2006.
- [12] W. K. Hastings. Monte Carlo sampling methods using Markov chains and their applications. *Biometrika*, 57(1):97–109, April 1970.
- [13] Tomáš Luber and Stanislav Sysala. Robust block diagonal preconditioners for poroelastic problems with strongly heterogeneous material. *Numerical Linear Algebra with Applications*, 31(3):e2546, 2024.

- [14] Mads B. Lykkegaard, Timothy J. Dodwell, Colin Fox, Georgios Mingas, and Robert Scheichl. Multilevel Delayed Acceptance MCMC. *SIAM/ASA Journal on Uncertainty Quantification*, 11(1):1–30, 2023.
- [15] Nicholas Metropolis, Arianna W. Rosenbluth, Marshall N. Rosenbluth, Augusta H. Teller, and Edward Teller. Equation of State Calculations by Fast Computing Machines. *The Journal of Chemical Physics*, 21(6):1087–1092, June 1953.
- [16] Radford M. Neal. MCMC using Hamiltonian dynamics. *Handbook of Markov Chain Monte Carlo*, pages 113–162, 2011.
- [17] Christopher J. Paciorek and Mark J. Schervish. Spatial modelling using a new class of nonstationary covariance functions. *Environmetrics*, 17(5):483–506, 2006.
- [18] Gareth O. Roberts and Jeffrey S. Rosenthal. Coupling and Ergodicity of Adaptive Markov Chain Monte Carlo Algorithms. *Journal of Applied Probability*, 44(2):458–475, June 2007.
- [19] Jonny Rutqvist, Lennart Börgesson, Masakazu Chijimatsu, Jan Hernelind, Lanru Jing, Akira Kobayashi, and Son Nguyen. Modeling of damage, permeability changes and pressure responses during excavation of the TSX tunnel in granitic rock at URL, Canada. *Environmental Geology*, 57(6):1263–1274, May 2009.
- [20] Chris Sherlock, Andrew Golightly, and Daniel A. Henderson. Adaptive, Delayed-Acceptance MCMC for Targets With Expensive Likelihoods. *Journal of Computational and Graphical Statistics*, 26(2):434–444, April 2017.